Supporting Information

Harkcom et al. 10.1073/pnas.1404269111

SI Materials and Methods

Reagents and Materials.

Reagent	Supplier	Catalog no.
Paclitaxel	Sigma-Aldrich	T1912
Vinblastine	Sigma-Aldrich	V1377
Colchicine	Sigma-Aldrich	9754
Nocodazole	Sigma-Aldrich	M1404
Vincristine	Sigma-Aldrich	V8879
Vindesine	Santa Cruz	Sc205883
Vinorelbine	Sigma-Aldrich	V2264
Jasplakinolide	EMD Biosciences	420127
Tubulin	Cytoskeleton	TL238
X-tremeGENE HP	Roche	6366244001
Nicotinamide adenine dinucleotide (NAD^+)	Affymetrix	19439
nicotinamide mononucleotide (NMN)	Sigma-Aldrich	N3501
Lactate dehydrogenase	Sigma-Aldrich	L7525
Diaphorase	Affymetrix	14615
CellROX Deep Red	Life Technologies	C10422
α-Tocopherol	Sigma-Aldrich	T3251
Ascorbic Acid	Sigma-Aldrich	A4544
MTT Assay	Roche	11465007001
Multitox Fluor Cytotoxicity Assay	Promega	G9200
Caspase-Glo 3/7 Assay	Promega	G8090
Alexa Fluor 568 Phalloidin	Life Technologies	A12380

Antibodies.

Antibody	Source	Catalog no.
Tyrosinated Tubulin	Novus Biologicals	NB600-506
Acetylated Tubulin	Sigma-Aldrich	T7451
α-Tubulin	GenScript	A01410
β-Actin	GenScript	A00702
Sirtuin-3 (SIRT3)	Cell Signaling	5490
Donkey Anti-Rat Alexa 488	Invitrogen	A-21206
Donkey Anti-Mouse HRP	GE Healthcare	NA931
Donkey Anti-Rabbit HRP	GE Healthcare	NA934

EB Comet Imaging Assays. MCF-7 cells were plated on 35-mm glass bottom No. 1.5 dishes (MatTek) and infected with GFP-EB1ΔC lentiviral particles. EB1ΔC (referred to throughout the manuscript as EB1 for simplicity) is an EB1 construct truncated at amino acid 248 that does not interact with other +TiP proteins (1). This construct had a better signal-to-noise ratio than full-length EB1, as determined empirically. The cells were imaged 2 d postinfection to measure the dynamicity of microtubules ends labeled with GFP-EB1ΔC. Cells were pretreated with vehicle (water) or 10 mM NAD^+ for 2 h at 37 °C before imaging. Images were acquired every 0.5 s for a total of 1 min for each time-lapse movie.

Dissociated embryonic day (E) 14.5 rat dorsal root ganglia (DRG) sensory neurons (~4×10^4 cells per device applied to the cell body compartment) were cultured in microfluidic devices on coated, glass-bottom dishes as described previously (2). EB3 imaging was performed using human EB3 following protocols described previously (3). The neurons were infected with GFP-EB3 lentiviral particles immediately after plating. On days in vitro (DIV) 4–5, the axonal compartment was imaged using live-cell confocal microscopy (as described below) to measure the dynamicity of microtubule ends labeled with GFP-EB3. When indicated, axons were transected by aspiration of the cell bodies. Images were acquired every 0.5 s for a total of 1 min for each time-lapse movie, and analysis was performed as described below.

Computational Analysis of MT Dynamics Using End-Binding Proteins. All image analysis was performed using ClusterTrack, an algorithm that has been described in detail previously (3, 4). In brief, this approach can track thousands of end-binding (EB)-EGFP comets that are visible in images within a time-lapse sequence. Imaging these comets allows the detection of spatial patterns of MT dynamics. The algorithm uses spatiotemporal clustering of EB-EGFP growth tracks to infer MT behaviors during phases of pausing and shortening. EB comet detection is accomplished by band-pass filtering, which enhances image features that have the expected size of an EB comet. This approach reduces higher-frequency noise and lower-frequency structures that represent larger aggregates of fluorescent protein. The algorithm is robust against variations in comet lengths, both within videos and between videos. The feature detector delivers not only the position of each comet in a frame but also the eccentricity and orientation of the comets. The latter is used as a directional cue in the subsequent tracking of comets from one frame to the next.

The cost of an individual assignment is defined in statistical terms as the Mahalanobis distance between projected and extracted comets. Detected EB-EGFP comets are tracked using a Kalman filter-based multiobject tracking algorithm (5). Clustering of colinear growth tracks that likely belong to the same microtubule is performed by solving a linear assignment problem (6), which identifies the globally optimal positional correspondences between the endpoints of terminating tracks and the start points of newly initiated tracks. Every potential assignment is characterized by a cost of linking. A pairing between a track termination and a track initiation is considered only if these two events are separated by less than 15 s or another user-specified time-lag.

Furthermore, the track initiation has to fall within either one of two cone-shaped, geometrical search regions. The choice of the forward cone with an opening half-angle of 60° is motivated by the observation that during pauses or out of focus movements, microtubules sometimes undergo significant lateral displacements and directional changes, especially at the cell periphery. The longer the gap duration, the larger is the probability for a lateral step and directional change. In contrast, the backward cone has an opening half-angle of 10° only, motivated by the observation that microtubule rescues generally follow the growth track before the catastrophe. By construction, this assignment is spatially and temporally global, which leads to a high level of robustness. Competing pairings are weighed against one another via a cost function that prefers colinear track parings with a short gap distance.

Parameters in ClusterTrack were as follows: s1 = 1.25, s2 = 3.5, k1 = 3.5, k2 = 1, search radius = 7.5 pixels. Remaining conditions were set to defaults. Accuracy of comet tracking was verified by visual inspection of time-lapse movies. All parameters were calculated per cell. For each condition, 15 videos containing one or two cells are acquired. For statistical analysis, we used a permutation t test (200 repetitions), which makes no assumptions about normality of the data, to compare differences in the mean parameter values (4).

Preparation of Microfluidic Devices for Compartmentalization of Axons. The polydimethylsiloxane microfluidic devices with 450-μm

microgrooves were prepared as described previously (2, 7). The devices were cleaned, sterilized, and reversibly affixed to plastic tissue culture dishes (Corning) coated with poly-L-lysine (Trevigen) and 5 $\mu g/mL^{-1}$ laminin (Trevigen).

Compartmentalized Neuronal Culture in Microfluidic Devices. DRG neurons and explants were prepared as described previously (8, 9). A total of 150 μL per reservoir of DRG culture medium [Neurobasal supplemented with 2% (vol/vol) B27 (Invitrogen), 2 mM Glutamax (Invitrogen), 1× penicillin/streptomycin (Invitrogen), 10 μM 5-fluorodeoxyuridine (Sigma), and 50 ng/mL^{-1} 2.5S NGF (Invitrogen)] was added to the distal axonal compartment followed by plating ~4×10^4 dissociated E14.5 rat DRG neurons in the cell body compartment. After a 15 min incubation to allow neuronal attachment to the tissue culture dishes, culture medium was added to the cell body compartment.

Taxol-Mediated Axon Protection in Compartmentalized Chambers. Dissociated E14.5 rat DRG neurons (~4×10^4 cells per device applied to the cell body compartment) were cultured in microfluidic devices on coated plastic dishes. On DIV5, taxol (1 μM) was added to the axonal compartment. The cells were then transected by flushing the cell bodies from the cell body compartment by aspiration. The compartment was flushed twice with PBS to ensure all cell bodies were removed. Removal of cell bodies was confirmed by inspecting the cell body compartment by phase-contrast microscopy. Phase-contrast images (20× objective) of the distal axonal compartment were acquired at the indicated time points. Axon degeneration was analyzed by calculating the degeneration index, as previously described (100 axons from three fields per condition) (10). Briefly, following background subtraction to improve the accuracy of thresholding, the phase-contrast images were thresholded and converted to binary images. The total axonal area was defined as the number of black pixels. As degenerated axons acquire a particulate structure because of fragmentation, degeneration was detected using the particle analyzer module in Fiji (11). The degeneration index is the ratio of particulate axonal area over total axon area.

Transection Assay in DRG Explant Cultures. E14.5 rat DRG explants were plated (one per well) in coated 24-well plastic dishes. On DIV5, the axons were transected using a pipette tip to remove the cell bodies. Immediately after transection, 1 μM taxol or vehicle (DMSO) was added, and phase-contrast images (20× objective) of the axons were acquired. The extent of axon degeneration was determined by calculating the degeneration index as described above (100 axons from three fields per condition) (10).

In Vitro Tubulin Polymerization Assay. The assay was performed as per the manufacturer's (Cytoskeleton, BK006P) instructions. Briefly, purified bovine tubulin (3 mg/mL) in tubulin polymerization buffer (80 mM Pipes pH 6.9, 2 mM $MgCl_2$, 0.5 mM EGTA, and 3% glycerol) was mixed with 10 mM NAD^+, 10 μM taxol, or DMSO in a half-area 96-well plate. Absorbance at 340 nm was monitored for 1 h. An increase in absorbance indicates an increase in polymerized tubulin. Two technical replicates were performed for each of three independent experiments.

Live-Cell Protease Viability Assay. To assess cell viability, we used the MultiTox-Fluor Multiplex Cytotoxicity Assay (Promega G9200) according to the manufacturer's protocol. Briefly, we plated 10,000–15,000 cells in a 96-well plate and treated the cells with the indicated compounds. After culturing for the indicated amount of time, we added the viability/cytotoxicity reagent, glycyl-phenylalanyl-aminofluorocoumarin (GF-AFC). The substrate enters intact cells, where it is cleaved by a live-cell protease to generate a fluorescent compound. Upon loss of cell-membrane integrity, the protease becomes inactive, and is thus used as a marker for cell viability. Cells were incubated with the reagent for 45 min at 37 °C, and fluorescence was measured at $400_{ex}/505_{em}$.

MTT Viability Assay. As an alternative cell viability assay, we used the MTT Cell Proliferation Kit (Roche 11 465 007 001) according to the manufacturer's protocol. Briefly, we plated ~5,000 cells in a 96-well plate and treated the cells with the indicated compounds. After culturing for the indicated time, we added the MTT labeling reagent to a final concentration of 0.5 mg/mL and incubated for 4 h at 37 °C. We then added solubilization buffer and incubated over night at 37 °C. Finally, we measured absorbance at 570 nm with a 680-nm reference wavelength. This assay measures the conversion of MTT, a tetrazolium dye, to insoluble formazan, which only occurs in metabolically active cells.

Apoptosis Assay. To measure apoptosis, we used the Caspase-Glo 3/7 assay (Promega G8090) according to the manufacturer's protocol. Briefly, we plated 10,000–15,000 cells in a 96-well plate and treated the cells with the indicated compounds. After culturing for the indicated amount of time, we added the caspase-3/-7 substrate, which contains the tetrapeptide sequence DEVD. Caspase cleavage of the substrate produces a luminescent signal. After a 45-min incubation, we monitored luminescence as a readout of apoptosis.

Reactive Oxygen Species Assay. To measure reactive oxygen species (ROS) levels, we used the CellROX Deep Red Reagent (Life Technologies C10422) according to the manufacturer's protocol. Briefly, we plated ~10,000 cells in a 96-well plate and added the appropriate treatments. After incubating, we added the CellROX reagent along with Hoechst 3334 dye (1 μg/mL), incubated for 30 min at 37 °C, and washed twice with warm PBS. Afterward, fluorescence was monitored at $350_{ex}/461_{em}$ (Hoechst) and $640_{ex}/665_{em}$ (CellROX). ROS signal was normalized to cell number (Hoechst signal).

Western Blotting. Cells were lysed in RIPA buffer (50 mM Tris·HCl pH 8.0, 150 mM NaCl, 1% Nonidet P-40, 0.5% sodium deoxycholate, 0.1% SDS, and 1× Roche protease inhibitor mixture) and sonicated. Any remaining insoluble debris was pelleted, and the supernatant was saved. Proteins were resolved by 4–12% SDS/PAGE and transferred to a PVDF membrane. The membrane was blocked with 3% (wt/vol) nonfat milk in PBS containing 0.05% Tween-20 (PBST), probed with primary and secondary antibodies in 1% nonfat milk in PBST, and detected using ECL Prime reagent (GE Healthcare). Images were acquired using a ChemiDoc MP system and Image Lab software version 4.0.1 (Bio-Rad Laboratories). Quantification was performed using Image Lab.

Image Acquisition and Data Analysis. Fluorescent and phase-contrast images were acquired on a Nikon Eclipse TE2000-E microscope equipped with a CoolSnap HQ2 CCD camera. Within each experiment, exposure times were kept constant and in the linear range throughout. Phase images were acquired using a 20× Ph1 ADL (NA = 0.4) air objective. Fluorescent images were acquired using a 60× Plan-Apochromat (NA = 1.4) oil-immersion objective. Stacks of images were taken and 3D deconvolution was performed using AutoDeblur X (Media Cybernetics). Fixed sample images were taken at 25 °C, and live cell images were taken at 37 °C in an environmental chamber containing 5% CO_2(g). Images were acquired using NIS-Elements Advanced Research v3.1 software (Nikon), and data analysis was performed using Fiji (11), GraphPad Prism version 5.0 (GraphPad Software), and MATLAB (MathWorks).

Live-cell confocal microscopy was performed with a Hamamatsu Orca R2 camera (Middlesex) mounted onto a CSU-X1 (Yokogawa Electric Corporation) spinning disk head on a Zeiss SD Observer I equipped with a 100× Plan-Apochromat (NA = 1.46) oil objective (Carl Zeiss).

1. Gierke S, Wittmann T (2012) EB1-recruited microtubule +TIP complexes coordinate protrusion dynamics during 3D epithelial remodeling. *Curr Biol* 22(9):753–762.
2. Hengst U, Deglincerti A, Kim HJ, Jeon NL, Jaffrey SR (2009) Axonal elongation triggered by stimulus-induced local translation of a polarity complex protein. *Nat Cell Biol* 11(8):1024–1030.
3. Matov A, et al. (2010) Analysis of microtubule dynamic instability using a plus-end growth marker. *Nat Methods* 7(9):761–768.
4. Thoma CR, et al. (2010) Quantitative image analysis identifies pVHL as a key regulator of microtubule dynamic instability. *J Cell Biol* 190(6):991–1003.
5. Yang G, Matov A, Danuser G (2005) Reliable tracking of large scale dense antiparallel particle motion for fluorescence live cell imaging. *Proc IEEE Conf Comput Vis Pattern Recognit*, 10.1109/CVPR.2005.519.
6. Schrijver A (2003) *Combinatorial Optimization: Polyhedra and Efficiency* (Google eBook) (Springer, Berlin), Vol 1.
7. Taylor AM, et al. (2005) A microfluidic culture platform for CNS axonal injury, regeneration and transport. *Nat Methods* 2(8):599–605.
8. Wu KY, et al. (2005) Local translation of RhoA regulates growth cone collapse. *Nature* 436(7053):1020–1024.
9. Cohen MS, Ghosh AK, Kim HJ, Jeon NL, Jaffrey SR (2012) Chemical genetic-mediated spatial regulation of protein expression in neurons reveals an axonal function for wld(s). *Chem Biol* 19(2):179–187.
10. Sasaki Y, Vohra BPS, Lund FE, Milbrandt J (2009) Nicotinamide mononucleotide adenylyl transferase-mediated axonal protection requires enzymatic activity but not increased levels of neuronal nicotinamide adenine dinucleotide. *J Neurosci* 29(17): 5525–5535.
11. Schindelin J, et al. (2012) Fiji: An open-source platform for biological-image analysis. *Nat Methods* 9(7):676–682.

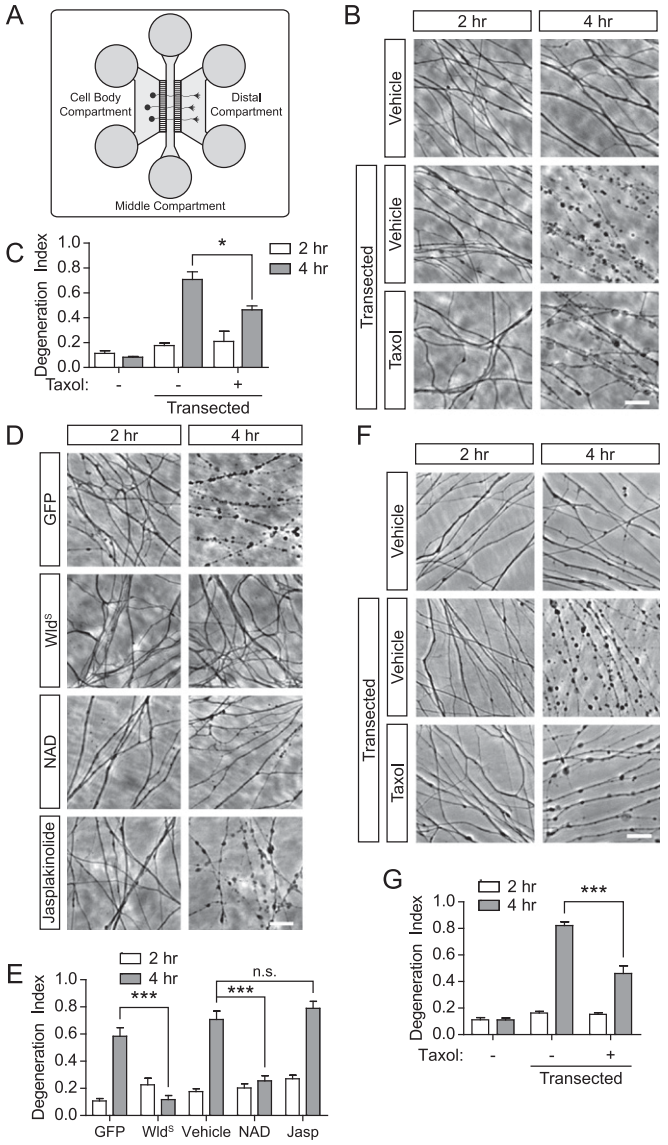

Fig. S1. Microtubule stabilization protects from axonal degeneration. (*A*) Schematic of microfluidic chambers. We used microfluidic chambers for culturing neurons primarily because it provides a simple, consistent way to transect axons and monitor axonal degeneration, while also allowing us to efficiently infect all neurons with lentivirus. Dissociated neurons are readily infected in a homogeneous manner. We therefore performed many of our experiments using neurons cultured in microfluidic devices. In this culturing system, neurons are applied to the cell body compartment (left side of image), and axons spontaneously grow through the 5-μm-wide, 450-μm-long microgrooves into the central compartment, and then through to the distal compartments (indicated). Our laboratory has used these devices extensively (1–5). After axons grow through the grooves, the cell bodies can be sheared off the axons by flushing buffer through the cell body compartment. This transection protocol initiates axonal degeneration. (*B*) Taxol delays axon degeneration. Compounds that affect diverse signaling pathways were screened for their effect of axonal degeneration. In these experiments, dissociated rat E14.5 DRG neurons were cultured in microfluidic chambers. On DIV5, axons were transected by flushing buffer through the cell body compartment, which washes away the cell bodies. Axons in the distal compartment were imaged 2 h and 4 h posttransection. In control, untransected neurons, axons appear morphologically intact at all time points. In transected neurons, axons appear intact at 2 h, but blebbing and fragmentation are seen by 4 h. Application of taxol (1 μM) to the axonal compartment at the time of transection markedly reduces axonal degeneration at 4 h. This finding suggests that stabilization of microtubules delays axon degeneration. (*C*) Quantification of axon degeneration in *B*. Degeneration index was calculated in Fiji (6) by first thresholding each image and measuring the total axonal area. Then, images were thresholded using the particle analyzer, which selects axonal fragments but not linear sections, and the ratio of axon fragments to total axon area is referred to as the degeneration index (7). For each condition, three nonoverlapping images were acquired for $n = 3$ replicates. Bar graph represents mean ± SEM $P < 0.05$; $^{**}P < 0.01$ (one-way ANOVA with Tukey's post hoc test). (*D*) NAD^+ treatment and expression of Wallerian degeneration slow (Wld^S) protein, but not treatment with stabilizers of actin polymers, delay axonal degeneration. We wondered if the axon-protective effect of taxol could be recapitulated by any compound that stabilizes the cytoskeleton. To test this, we used the actin stabilizer, jasplakinolide (50 nM). E14.5 DRG neurons were cultured in microfluidic chambers and transected at DIV4, and phase-contrast images were acquired at 2 and 4 h. As can be seen in control axons, degeneration is evident at 4 h, and this is blocked by expression of Wld^S or by treatment with NAD^+ (5 mM), as expected. However, treatment with jasplakinolide failed to delay axonal degeneration. These data support the idea that there is a unique role for microtubules in regulating the onset of axonal degeneration. (*E*) Quantification of the results in *D*. Vehicle control results from *B* are included for clarity. For each condition, three nonoverlapping images were acquired for $n = 3$ replicates. Bar graph represents mean ± SEM; $^{***}P < 0.001$ (one-way ANOVA with Tukey's post hoc test). (*F*) The axon-protective effects of taxol are seen in DRG explant cultures. In *B* and *C*, we show that taxol delays axonal degeneration using DRG neurons prepared in microfluidic chambers. However, we sought to confirm that taxol has the same effect in the more widely used explant culture model of axonal degeneration. E14.5 rat DRG explants were cultured for 4

Legend continued on following page

DIV, and then axons were transected and the explant was removed, resulting in removal of the cell bodies. Axons remain on the plastic. As can be seen, no degeneration occurs in untransected axons at either 2 or 4 h. However, in transected axons, significant degeneration is observed by 4 h. This effect was blocked by inclusion of taxol (1 μM) at the time of transection. Thus, taxol delays axonal degeneration in both explant cultures and microfluidic chambers. It should be noted that unlike Wld^S, which exhibits a persistent axonal protection that lasts at least 24 h (8, 9), the effects of taxol are lost by 8 h in these cultures. Taxol is known to have its own axon degeneration-inducing effects (10). Thus, we suspect that taxol transiently protects axons, but the overall impairment of microtubule dynamics eventually elicits axon degeneration on its own. (*G*) Quantification of results in *F*. For each condition, three nonoverlapping images were acquired for $n = 3$ replicates. Bar graph represents mean ± SEM; ***$P < 0.001$ (one-way ANOVA with Tukey's post hoc test). (Scale bars, 20 μm in *B*, *D*, and *F*.)

1. Hengst U, Deglincerti A, Kim HJ, Jeon NL, Jaffrey SR (2009) Axonal elongation triggered by stimulus-induced local translation of a polarity complex protein. *Nat Cell Biol* 11(8):1024–1030.
2. Cohen MS, Ghosh AK, Kim HJ, Jeon NL, Jaffrey SR (2012) Chemical genetic-mediated spatial regulation of protein expression in neurons reveals an axonal function for wld(s). *Chem Biol* 19(2):179–187.
3. Cohen MS, Bas Orth C, Kim HJ, Jeon NL, Jaffrey SR (2011) Neurotrophin-mediated dendrite-to-nucleus signaling revealed by microfluidic compartmentalization of dendrites. *Proc Natl Acad Sci USA* 108(27):11246–11251.
4. Walker BA, et al. (2012) Reprogramming axonal behavior by axon-specific viral transduction. *Gene Ther* 19(9):947–955.
5. Ji S-J, Jaffrey SR (2012) Intra-axonal translation of SMAD1/5/8 mediates retrograde regulation of trigeminal ganglia subtype specification. *Neuron* 74(1):95–107.
6. Schindelin J, et al. (2012) Fiji: An open-source platform for biological-image analysis. *Nat Methods* 9(7):676–682.
7. Sasaki Y, Vohra BPS, Lund FE, Milbrandt J (2009) Nicotinamide mononucleotide adenylyl transferase-mediated axonal protection requires enzymatic activity but not increased levels of neuronal nicotinamide adenine dinucleotide. *J Neurosci* 29(17):5525–5535.
8. Araki T, Sasaki Y, Milbrandt J (2004) Increased nuclear NAD biosynthesis and SIRT1 activation prevent axonal degeneration. *Science* 305(5686):1010–1013.
9. Wang J, et al. (2005) A local mechanism mediates NAD-dependent protection of axon degeneration. *J Cell Biol* 170(3):349–355.
10. Wang MS, Davis AA, Culver DG, Glass JD (2002) WldS mice are resistant to paclitaxel (taxol) neuropathy. *Ann Neurol* 52(4):442–447.

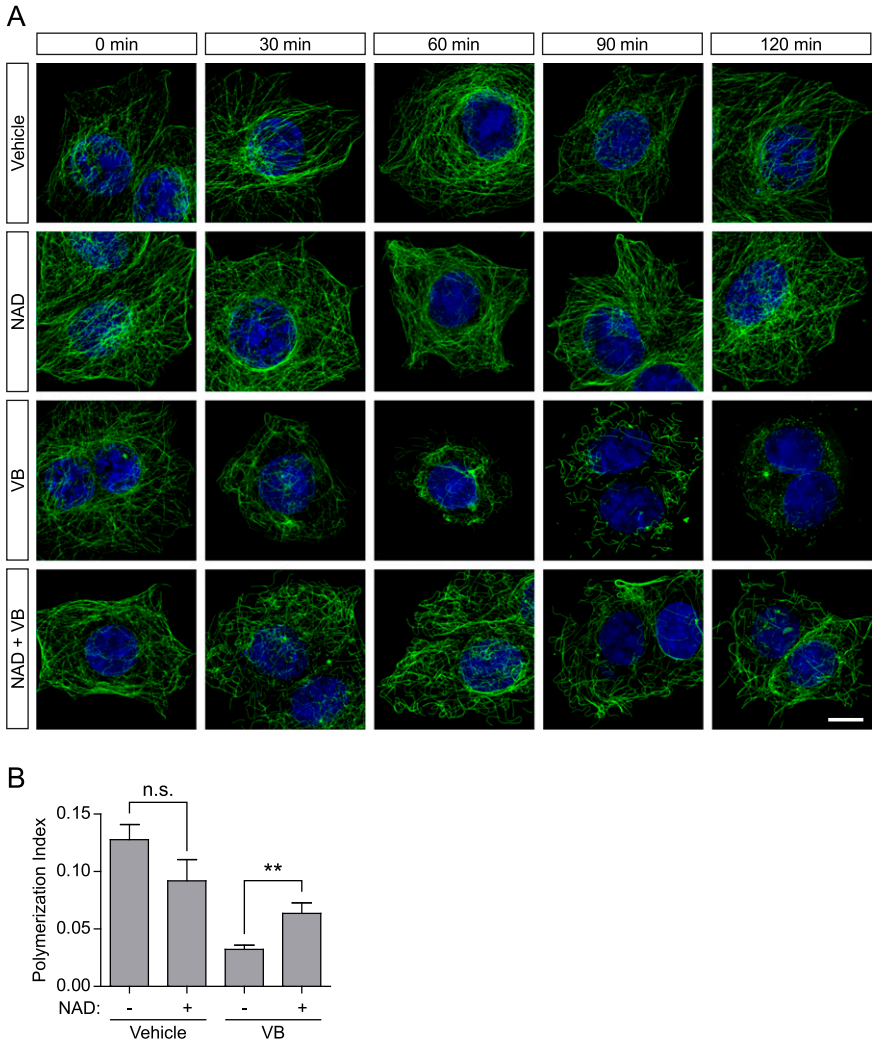

Fig. S2. NAD^+ prevents the microtubule depolymerization effect of vinblastine. (*A*) NAD^+ exhibits a microtubule-protective effect. This figure is identical to Fig. 1*B*, except more time points are included. As can be seen, treatment with NAD^+ (5 mM) blocks the microtubule destabilizing effects of vinblastine (100 nM) in MCF-7 cells. Microtubule polymers were measured by anti–Tyr-tubulin immunostaining (green). (Scale bar, 10 μm.) (*B*) NAD^+ exhibits a microtubule-protective effect in multiple cell types. To confirm that our results were not unique to MCF-7 cells, we performed the same experiment in HEK293T cells. Cells treated with vinblastine (50 nM) exhibited a complete loss of microtubules by 2 h. Coapplication of NAD^+ (5 mM), however, blocks the microtubule destabilizing effects of vinblastine. To quantify microtubule polymer mass, polymerized microtubules were identified and binarized using the Tubeness plugin in Fiji, which identifies linear structures. The total area of the cell was determined using an Alexa Fluor 568 Phalloidin counterstain, and the graph represents the ratio of microtubule polymers to cell area, which we refer to as the polymerization index. To remove background fluorescence caused by depolymerized tubulin, soluble tubulin was extracted before fixation. These results confirm that the microtubule protective effect of NAD^+ is not specific to one cell type. We measured ~100 cells from $n = 3$ replicates. Bar graph represents mean ± SEM; n.s. not significant; $^{**}P < 0.01$ (unpaired, two-tailed Student *t* test).

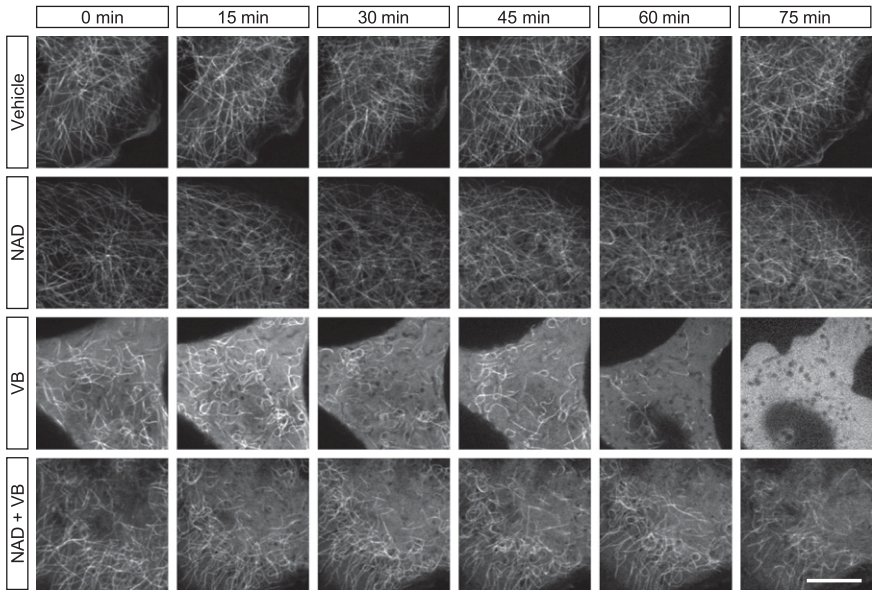

Fig. S3. NAD^+ prevents the microtubule depolymerization effect of vinblastine. Live, time-lapse imaging of microtubules. To assess the ability of NAD^+ to alter microtubule polymer stability, we monitored microtubules by live time-lapse imaging of MCF-7 cells stably expressing GFP–α-tubulin. In these experiments, cells were pretreated with NAD^+ (5 mM) or vehicle (water) for 2 h, followed by time-lapse imaging for 90 min. In cells receiving vehicle treatment or NAD^+ alone, there were no obvious changes in microtubule polymer mass throughout the time course. In cells receiving vinblastine (VB; 25 nM) treatment, an initial loss of microtubule polymers was observed even in the short time period (~1 min) between adding the vinblastine and beginning imaging. Complete microtubule depolymerization was seen by 75 min. However, in cells that received NAD^+ treatment before the addition of vinblastine, we observed a significant protection of the microtubule polymer mass (Movies S1–S4). Taken together, these data indicate that NAD^+ protects microtubules from depolymerization elicited by vinblastine. Time-lapse images were acquired every 15 s for 90 min using a spinning disk confocal microscope (100× objective) equipped with an environmental chamber. Because of slight drift in the focal plane, ~one representative image was selected for each minute of the time course for the final movies. In addition, time-lapse movies were bleach-corrected and background subtracted in Fiji. Finally, for the vinblastine treatment movie, slight movement in the *x*–*y* plane was corrected using the warp-stabilizer function in After Effects (Adobe Systems). (Scale bar, 5 μm.)

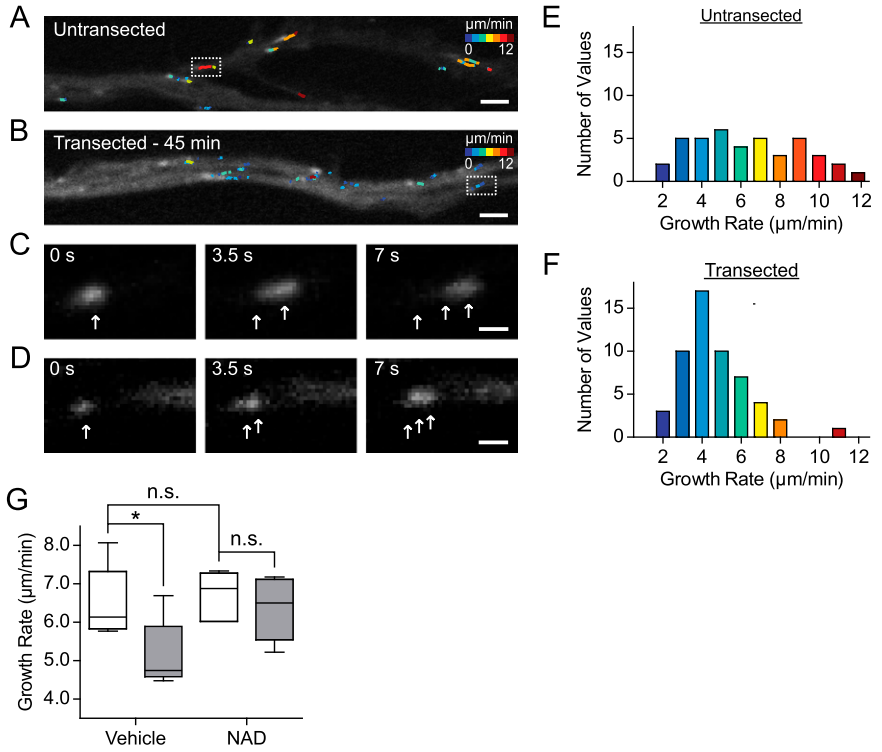

Fig. S4. NAD^+ prevents disruption of microtubule dynamics in transected axons. (*A–D*) The growth rate of GFP-EB3 comets is markedly reduced shortly after axonal transection. The velocity of a GFP-EB3 comet reflects the rate at which the plus end of the microtubule is growing by adding tubulin dimers. Individual comet tracks are shown overlaid onto an image of an axon bundle. The path of each comet is traced and colored based on its velocity (see heat map key). Time-lapse images were acquired before transection (*A*) or 45 min after transection (*B*), and for each time lapse, images were acquired every 0.5 s for a total of 2 min. Following axonal transection (*B*), the comet growth rate is markedly reduced. A single comet from each condition is highlighted to demonstrate the difference in growth rate (*C* and *D*). Note that the time stamps for *C* and *D* are normalized to 0 s. These comets were chosen because of their long lifetimes that facilitate comparison of growth rates. (Scale bars, 1 μm in *A* and *B* and 0.25 μm in *C* and *D*.) (*E* and *F*) Distribution of microtubule growth rates in a single axon before and 45 min after axon transection. The histograms show the frequency distribution of microtubule growth rates in a single axon. By 45 min posttransection, growth rates are significantly reduced (*F*) compared with uninjured axons (*E*), as measured by monitoring EB3-GFP comets. These data suggest microtubule polymerization is impaired by axonal transection. The colors correspond to the heat maps in *A* and *B*. (*G*) Box-and-whisker plot of microtubule growth rate before and after transection. The average microtubule growth rate per axon is significantly reduced 45 min after axonal transection in vehicle treated axons (6.56 ± 0.33 μm/min vs. 5.18 ± 0.31 μm/min). In neurons that are treated with NAD^+ (5 mM), microtubule growth rates are preserved following transection. NAD^+ treatment alone had a slight, but nonsignificant, increase in growth rate, similar to what is observed in MCF-7 cells (Fig. 2*E*). The smaller effect observed in axons is consistent with previous work demonstrating that microtubules in axons are highly stable (1). These data suggest NAD^+ can stabilize microtubules against injury-induced disruption, in agreement with our data from MCF-7 cells (Fig. 1 *B* and *C*). Approximately 30 movies were acquired for a total of ∼50 axon segments from three independent experiments. Box plots indicate the 25th percentile (bottom boundary), median (middle line), 75th percentile (top boundary), and nearest observations within 1.5-times the interquartile range (whiskers). n.s., not significant; $*P < 0.05$ (permutation *t* test).

1. Baas PW, Black MM (1990) Individual microtubules in the axon consist of domains that differ in both composition and stability. *J Cell Biol* 111(2):495–509.

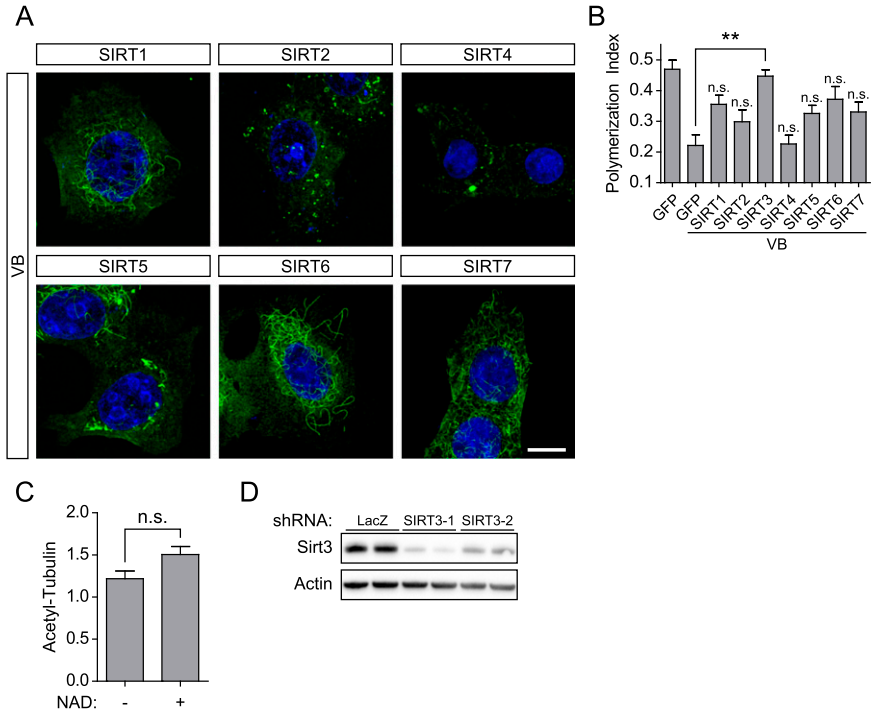

Fig. S5. SIRT3 mediates the microtubule stabilizing effects of NAD^+ in MCF-7 cells. (*A*) Expression of SIRT1, -2, -4, -5, -6, and -7 do not substantially protect the microtubule cytoskeleton from the effects of vinblastine. This experiment was performed along with the experiment presented in Fig. 5 *A* and *B*. Here we asked if any sirtuin could mimic the effect of NAD^+. Each sirtuin isoform was expressed in MCF-7 cells and microtubule polymer mass was measured by anti–Tyr-tubulin immunostaining (green) after vinblastine (VB; 100 nM) treatment for 2 h. In most cases, minor to moderate protective effects on microtubule polymers were seen upon sirtuin overexpression. In the case of SIRT1, this may reflect a SIRT1-dependent activation of SIRT3 via PGC-1α, as previously reported (1, 2). Because the effect of Wld^S and NAD^+ on axon degeneration is the result of an axonally localized target (3), nucleus-localized sirtuins, such as SIRT1, SIRT6, or SIRT7, are unlikely to be direct mediators of the effects of NAD^+ in axons. (Scale bar, 10 μm.) (*B*) Quantification of results in *A*. Microtubule polymer levels were quantified as described in Fig. 5*B*. SIRT3-GFP overexpression exhibited the most robust protective effect on microtubules. We measured ∼100 cells from $n = 3$ replicates. The bar graph shows the mean ± SEM. The GFP control and the SIRT3 results shown in Fig. 5*B* are included for clarity. n.s., not significant; $^{**}P < 0.01$ (one-way ANOVA with Tukey's post hoc test). (*C*) NAD^+ treatment does not alter levels of acetylated tubulin. To determine if NAD^+ treatment could be affecting SIRT2-mediated tubulin deacetylation, we measured levels of acetyl-lysine-40 on α-tubulin via Western blot. MCF-7 cells were treated with vehicle control or 5 mM NAD^+ for 2 h, the standard treatment time for our assays, and then processed for Western blotting. Following NAD^+ treatment, we did not observe a significant change in levels of acetylated-tubulin. These results suggest that SIRT2-mediated deacetylation of tubulin is not likely to account for the effects of NAD^+ on microtubule polymer stability. We measured acetylated-tubulin from $n = 3$ independent samples, and the bar graph represents the mean ± SEM; n.s., not significant; $P = 0.096$ (unpaired, two-tailed Student *t* test). (*D*) Validation of human SIRT3 shRNA constructs. Lentivirus expressing SIRT3 shRNA specific for human SIRT3 transcript were tested by infecting MCF-7 cells with the lentivirus and immunoblotting for endogenous SIRT3 levels. Western blots were performed 5 d after viral infection. At least three independent experiments were performed to confirm knockdown, and SIRT3 levels were reduced below 25% of control.

1. Rodgers JT, et al. (2005) Nutrient control of glucose homeostasis through a complex of PGC-1alpha and SIRT1. *Nature* 434(7029):113–118.
2. Kong X, et al. (2010) Sirtuin 3, a new target of PGC-1alpha, plays an important role in the suppression of ROS and mitochondrial biogenesis. *PLoS ONE* 5(7):e11707.
3. Cohen MS, Ghosh AK, Kim HJ, Jeon NL, Jaffrey SR (2012) Chemical genetic-mediated spatial regulation of protein expression in neurons reveals an axonal function for wld(s). *Chem Biol* 19(2):179–187.

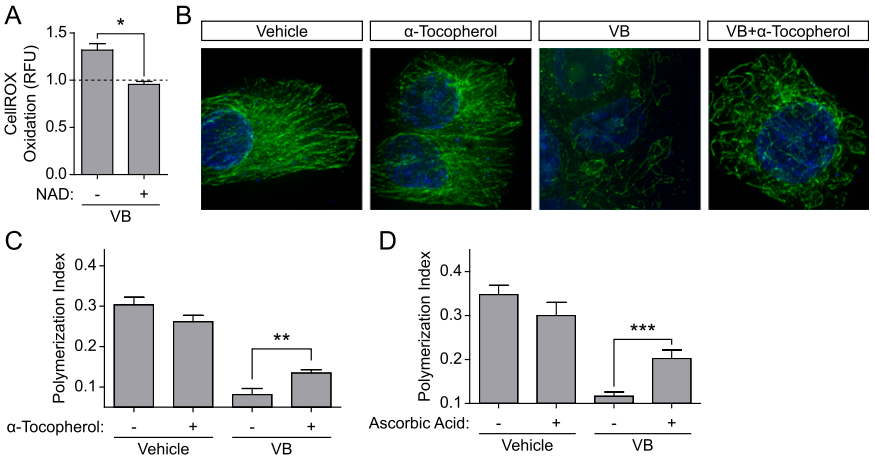

Fig. S6. Potential contribution of ROS to microtubule destabilization induced by vinblastine treatment. (*A*) NAD^+ prevents vinblastine-mediated increase in ROS. To determine if ROS might contribute to vinblastine-mediated microtubule destabilization, we first measured ROS levels in MCF-7 cells treated with vinblastine (100 nM) for 2 h. ROS levels were measured using CellROX Deep Red reagent, a dye that fluoresces when oxidized. Vinblastine treatment alone caused an ∼30% increase in ROS levels, as expected (1). When NAD^+ (5 mM) was present, however, there was a decrease in ROS levels. These data indicate that NAD^+ prevents the increase in ROS because of vinblastine. ROS levels were normalized to vehicle treatment or NAD^+ treatment alone. The dashed line represents baseline levels of ROS. We measured ∼10,000 cells per well in a 96-well plate from $n = 3$ replicates. It is important to note that quantification of ROS using CellROX and other similar reagents is semiquantitative, so the precise changes in ROS changes may be slightly different from the levels measured here. Bar graph represents mean ± SEM; $*P < 0.05$ (unpaired, two-tailed Student *t* test). (*B*) α-Tocopherol prevents vinblastine-mediated microtubule depolymerization. To determine if reducing ROS levels is sufficient to protect microtubules from depolymerization, MCF-7 cells were treated with vinblastine (100 nM) in the presence or absence of α-tocopherol (500 μM), a ROS scavenger. In the absence of α-tocopherol, vinblastine completely depolymerizes microtubules, as expected. When α-tocopherol is present, however, a significant portion of polymerized microtubules are preserved. These data suggest that reducing ROS levels is sufficient to stabilize microtubules and inhibit the depolymerizing effects of vinblastine, similar to that observed with NAD^+ treatment or SIRT3 overexpression. Microtubules were visualized by anti–Tyr-tubulin immunostaining (green). (Magnification: *B*, 60×.) (*C*) Quantification of results in *B*. To quantify microtubule polymer mass in MCF-7 cells, polymerized microtubules were identified and binarized using the Tubeness plugin in Fiji, which identifies linear structures. The total area of the cell was calculated using an Alexa Fluor 568 Phalloidin counterstain (not shown), and the graph represents the ratio of microtubule polymers to cell area, which we refer to as the polymerization index. We measured ∼100 cells from $n = 3$ replicates. Bar graph represents mean ± SEM; $**P < 0.01$ (unpaired, two-tailed Student *t* test). (*D*) Ascorbic acid prevents vinblastine-mediated microtubule depolymerization. We performed the same experiment in *B* using an alternative ROS scavenger, ascorbic acid. Similar to α-tocopherol, we found that ascorbic acid (10 mM) could protect a significant portion of polymerized microtubules from vinblastine-mediated depolymerization. These results are consistent with the idea that reducing ROS levels stabilizes microtubules. Quantification was performed as in *C*. Bar graph represents mean ± SEM; $***P < 0.001$ (unpaired, two-tailed Student *t* test).

1. Mahoney JR, Graf E (1986) Role of alpha-tocopherol, ascorbic acid, citric acid and EDTA as oxidants in model systems. *J Food Sci* 51(5):1293–1296.

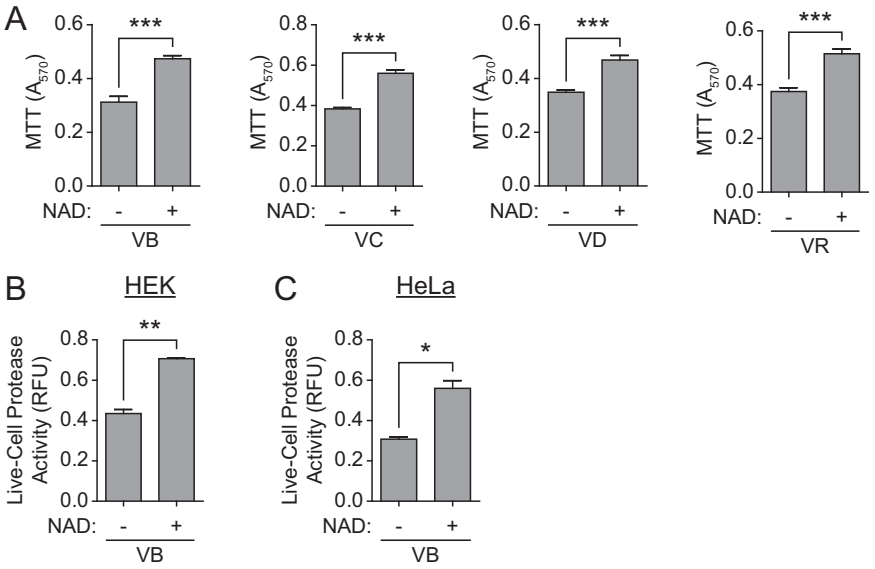

Fig. S7. NAD^+ reduces the sensitivity of cells to vinblastine. (*A*) NAD^+ antagonizes multiple microtubule-damaging agents. To confirm that our results are not specific to vinblastine, MCF-7 cells were treated with various microtubule damaging agents and viability was measured via an MTT assay. Treatment with vinblastine (100 nM; VB) caused a decrease in absorbance, a read-out of mitochondrial function and cell viability. When cells are treated with NAD^+ (5 mM) at the time of vinblastine application, there is a significant increase in cell viability, consistent with our previous results (Fig. 6*C*). We see the same effect when cells are treated with the structurally distinct vinca alkaloids vincristine (100 nM; VC), vindesine (100 nM, VD), and vinorelbine (100 nM; VR). These data further support our hypothesis that NAD^+ reduces the sensitivity of microtubule damaging agents. These data also further strengthen our hypothesis by using an alternative measure of cell viability. We measured ∼10,000 cells per well in a 96-well plate from $n = 3$ replicates. Bar graphs represent the mean ± SEM normalized to vehicle or NAD^+ control. ***$P < 0.001$ (unpaired, two-tailed Student *t* test). (*B* and *C*) Increased NAD^+ levels reduce sensitivity to vinblastine in multiple cell types. To confirm that our results are not specific to MCF-7 cells, we measured cell viability in HEK293T (*B*) and HeLa cells (*C*) via live-cell protease activity. Treatment with vinblastine (10 nM) for 48 h caused a decrease in cell viability, as expected. When cells are treated with NAD^+ (5 mM) at the time of vinblastine application, there is a significant increase in cell viability, consistent with our results in MCF-7 cells (Fig. 6*C*). These data demonstrate that increased NAD^+ levels can reduce the sensitivity of cells to vinblastine. We measured ∼10,000 cells per well in a 96-well plate from $n = 3$ replicates. Each point represents the mean ± SEM normalized to vehicle or NAD^+ control. *$P < 0.05$; **$P < 0.01$ (unpaired, two-tailed Student *t* test).

Table S1. NAD increases the dynamic instability of microtubules

	EB1-GFP expressing MCF-7 cells treated with:		
Image parameter	Vehicle	NAD (5 mM)	*t* test
No. of videos	11	11	
Growth speed (μm/min)	10.53 ± 1.70	12.87 ± 1.15	*
Gap speed (μm/min)	4.93 ± 0.87	6.15 ± 0.66	*
Segment growth speed (μm/min)	7.42 ± 1.26	9.14 ± 0.89	*
Track growth time (s)	8.11 ± 0.67	9.18 ± 0.65	NS
Segment growth time (s)	32.86 ± 2.31	32.99 ± 1.71	NS
Gap time (s)	10.68 ± 0.51	10.46 ± 0.54	NS
Time ratio gap/segment	0.38 ± 0.01	0.37 ± 0.01	NS
Shrink speed (μm/min)	8.85 ± 2.01	11.16 ± 1.55	*
Shrink time (s)	16.11 ± 0.71	16.57 ± 0.77	NS
Gaps per segment	1.29 ± 0.05	1.28 ± 0.04	NS
Shrink time (%)	0.23 ± 0.04	0.30 ± 0.04	*
Shrink probability (%)	0.31 ± 0.04	0.39 ± 0.03	*

EB1-GFP comets were analyzed using ClusterTrack. Segments are groups of growth tracks and gaps separated by a shrink event. Values represent the mean ± SD. Significance was determined using a one-tailed permutation *t* test of the means of the per cell numbers (200 repetitions). *$P < 0.05$; NS not significant.

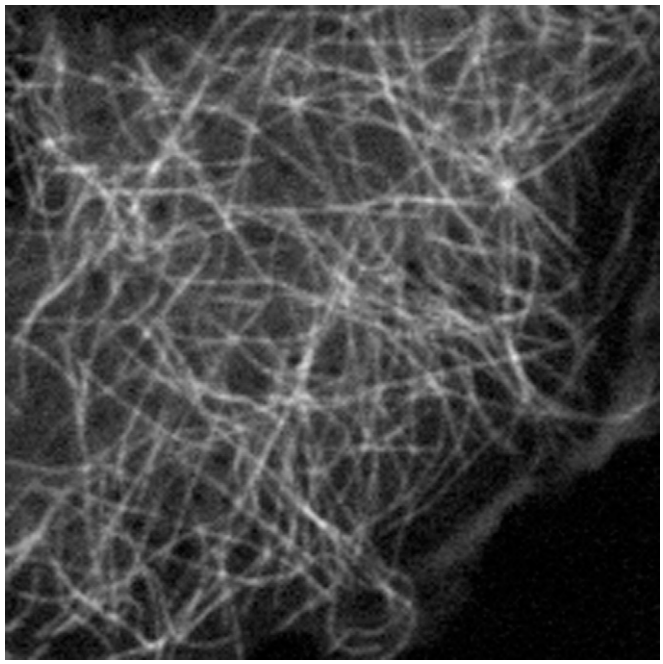

Movie S1. NAD^+ prevents the microtubule depolymerization effect of vinblastine. To assess the ability of NAD^+ to alter microtubule polymer stability, we monitored microtubules by live time-lapse imaging of MCF-7 cells stably expressing GFP–α-tubulin. In these experiments, cells were pretreated with NAD^+ (5 mM) or vehicle (water) for 2 h, followed by time-lapse imaging for 90 min. In cells receiving vehicle treatment there were no obvious changes in microtubule polymer mass throughout the time course. Taking the data from Movies S1–S4 together, we find that these data indicate that NAD^+ protects microtubules from depolymerization elicited by vinblastine. Time-lapse images were acquired every 15 s for 90 min using a spinning disk confocal microscope (100× objective) equipped with an environmental chamber. Because of slight drift in the focal plane, ∼one representative image was selected for each minute of the time course for the final movies. In addition, time-lapse movies were bleach-corrected and background subtracted in Fiji. Single images from the time-lapse movies are shown in Fig. S3 to facilitate comparisons.

Movie S1

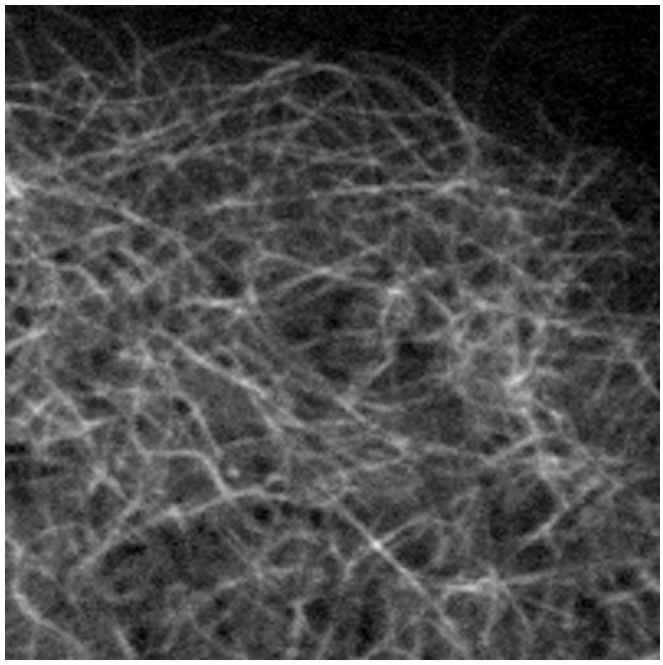

Movie S2. NAD^+ prevents the microtubule depolymerization effect of vinblastine. To assess the ability of NAD^+ to alter microtubule polymer stability, we monitored microtubules by live time-lapse imaging of MCF-7 cells stably expressing GFP–α-tubulin. In these experiments, cells were pretreated with NAD^+ (5 mM) or vehicle (water) for 2 h, followed by time-lapse imaging for 90 min. Taken together, the data from these four experiments indicate that NAD^+ protects microtubules from depolymerization elicited by vinblastine. Time-lapse images were acquired every 15 s for 90 min using a spinning disk confocal microscope (100× objective) equipped with an environmental chamber. Because of slight drift in the focal plane, ∼one representative image was selected for each minute of the time course for the final movies. In addition, time-lapse movies were bleach-corrected and background subtracted in Fiji. Single images from the time-lapse movies are shown in Fig. S3 to facilitate comparisons.

Movie S2

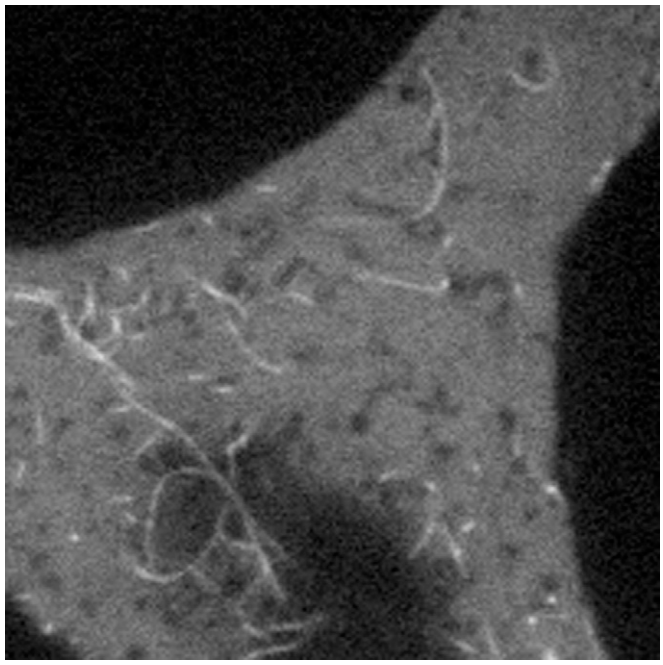

Movie S3. NAD^+ prevents the microtubule depolymerization effect of vinblastine. To assess the ability of NAD^+ to alter microtubule polymer stability, we monitored microtubules by live time-lapse imaging of MCF-7 cells stably expressing GFP–α-tubulin. In these experiments, cells were pretreated with NAD^+ (5 mM) or vehicle (water) for 2 h, followed by time-lapse imaging for 90 min. In cells receiving vinblastine (VB; 25 nM) treatment, an initial loss of microtubule polymers was observed even in the short time period (~1 min) between adding the vinblastine and beginning imaging. Complete microtubule depolymerization was seen by 75 min. Taken together, the data from these four experiments indicate that NAD^+ protects microtubules from depolymerization elicited by vinblastine. Time-lapse images were acquired every 15 s for 90 min using a spinning disk confocal microscope (100× objective) equipped with an environmental chamber. Because of slight drift in the focal plane, ~one representative image was selected for each minute of the time course for the final movies. In addition, time-lapse movies were bleach-corrected and background subtracted in Fiji. Finally, for the vinblastine-treatment movie, slight movement in the *x*–*y* plane was corrected using the warp-stabilizer function in After Effects (Adobe Systems). Single images from the time-lapse movies are shown in Fig. S3 to facilitate comparisons.

Movie S3

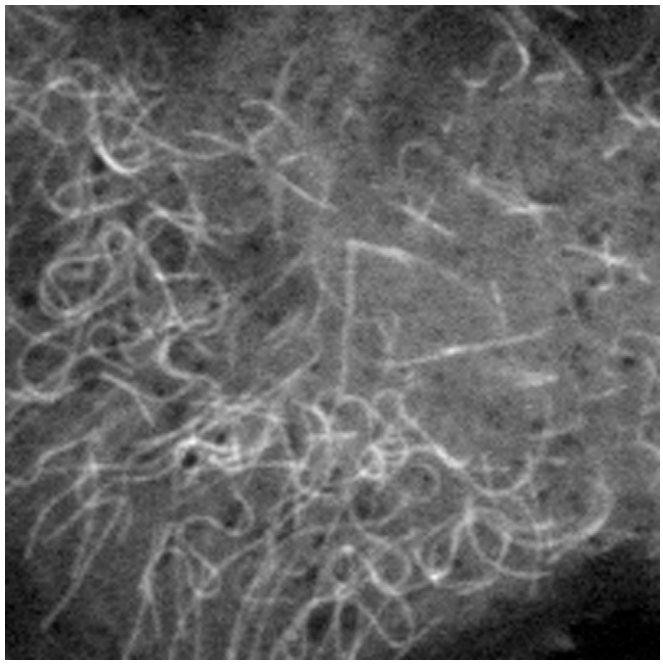

Movie S4. NAD^+ prevents the microtubule depolymerization effect of vinblastine. To assess the ability of NAD^+ to alter microtubule polymer stability, we monitored microtubules by live time-lapse imaging of MCF-7 cells stably expressing GFP–α-tubulin. In these experiments, cells were pretreated with NAD^+ (5 mM) or vehicle (water) for 2 h, followed by time-lapse imaging for 90 min. In cells receiving that received NAD^+ treatment before the addition of vinblastine, we observed a significant protection of the microtubule polymer mass. Taken together, the data from the experiments shown in Movies S1–S4 indicate that NAD^+ protects microtubules from depolymerization elicited by vinblastine. Time-lapse images were acquired every 15 s for 90 min using a spinning disk confocal microscope (100× objective) equipped with an environmental chamber. Because of slight drift in the focal plane, ∼one representative image was selected for each minute of the time course for the final movies. In addition, time-lapse movies were bleach-corrected and background subtracted in Fiji. For the vinblastine-treatment movie, slight movement in the *x*–*y* plane was corrected using the warp-stabilizer function in After Effects (Adobe Systems). Single images from the time-lapse movies are shown in Fig. S3 to facilitate comparisons.

Movie S4